

Three-Dimensional Evolution of Flux-Rope CMEs and Its Relation to the Local Orientation of the Heliospheric Current Sheet

A. Isavnin · A. Vourlidas · E.K.J. Kilpua

Received: 7 November 2013 / Accepted: 24 December 2013
© Springer Science+Business Media Dordrecht 2014

Abstract Flux ropes ejected from the Sun may change their geometrical orientation during their evolution, which directly affects their geoeffectiveness. Therefore, it is crucial to understand how solar flux ropes evolve in the heliosphere to improve our space-weather forecasting tools. We present a follow-up study of the concepts described by Isavnin, Vourlidas, and Kilpua (*Solar Phys.* **284**, 203, 2013). We analyze 14 coronal mass ejections (CMEs), with clear flux-rope signatures, observed during the decay of Solar Cycle 23 and rise of Solar Cycle 24. First, we estimate initial orientations of the flux ropes at the origin using extreme-ultraviolet observations of post-eruption arcades and/or eruptive prominences. Then we reconstruct multi-viewpoint coronagraph observations of the CMEs from ≈ 2 to $30 R_{\odot}$ with a three-dimensional geometric representation of a flux rope to determine their geometrical parameters. Finally, we propagate the flux ropes from $\approx 30 R_{\odot}$ to 1 AU through MHD-simulated background solar wind while using *in-situ* measurements at 1 AU of the associated magnetic cloud as a constraint for the propagation technique. This methodology allows us to estimate the flux-rope orientation all the way from the Sun to 1 AU. We find that while the flux-rope deflection occurs predominantly below $30 R_{\odot}$, a significant amount of deflection and rotation happens between $30 R_{\odot}$ and 1 AU. We compare the flux-rope orientation to the local orientation of the heliospheric current sheet (HCS). We find that slow flux ropes tend to align with the streams of slow solar wind in the inner heliosphere. During the solar-cycle minimum the slow solar-wind channel as well as the HCS usually occupy the area in the vicinity of the solar equatorial plane, which in the past led researchers to the hypothesis that flux ropes align with the HCS. Our results show that exceptions from this rule are explained by interaction with the Parker-spiraled background magnetic field, which dominates over the magnetic interaction with the HCS in the inner heliosphere at least during solar-minimum conditions.

A. Isavnin (✉) · E.K.J. Kilpua
Department of Physics, University of Helsinki, P.O. Box 64, 00014, Helsinki, Finland
e-mail: Alexey.Isavnin@helsinki.fi

A. Vourlidas
Space Science Division, Naval Research Laboratory, Washington, DC, USA

Keywords Coronal mass ejections, interplanetary · Magnetic fields, interplanetary · Magnetic fields, models

1. Introduction

Coronal mass ejections (CMEs) are the main drivers of space weather (*e.g.* Tsurutani *et al.*, 1988; Huttunen *et al.*, 2002; Zhang *et al.*, 2007), and thus forecasting their structures at 1 AU is essential. However, we do not yet possess detailed knowledge about the way CMEs evolve after their eruption from the Sun. The only mechanism of CME eruption that we know so far is via the ejection of a flux rope from the Sun (Chen, 2011). The majority of CMEs are thus believed to have flux ropes at their cores. However, only about 40 % of observed CMEs exhibit well-defined flux-rope signatures and can be called flux-rope CMEs (FR-CMEs: Vourlidas *et al.*, 2012). We will leave aside the question of whether all CMEs are FR-CMEs and focus on another important aspect of this phenomenon, which is the evolution of flux ropes after their ejection from the Sun. When discussing CMEs we will refer to FR-CMEs.

The flux-rope evolution can be decomposed into expansion, latitudinal and longitudinal deflections, rotation, and distortion, where the set of latitudinal and longitudinal deflections and rotation describes the change of global orientation of a flux rope. Geometrically all of these components are coupled together and are hard to study separately (Nieves-Chinchilla *et al.*, 2012). For instance, neglecting the possible deflections of a flux rope would affect our perception of its rotation or *vice versa*. That means that the only way to reliably study the geometrical evolution of a flux rope is by treating it as a three-dimensional (3D) object from the start.

The evolution of a flux rope directly affects its geomagnetic effectiveness. Deflections may cause a limb CME to hit the Earth or a halo CME to miss the Earth. Rotation of a flux rope, which is about to hit the Earth can change the efficiency of magnetic reconnection between the flux rope and the magnetosphere of the Earth, thus altering the geoeffectiveness of the impact.

The CME evolution is associated with its interaction with the magnetic field of the Sun and with the background solar wind and/or surrounding magnetic structures embedded in the solar wind. Wang *et al.* (2004) suggested that the longitudinal deflection of CMEs may be explained by the interaction with Parker-spiral-structured solar wind. Slow CMEs are pushed by faster solar wind thus feeling a westward component of force while fast CMEs are blocked by slower solar wind thus feeling an eastward component of force. Gopalswamy *et al.* (2009) suggested that driverless shocks detected at Earth with associated CMEs that originated from the central solar meridian can be explained by the kinematic interaction of CMEs with nearby coronal holes that deflected CMEs away from the Sun–Earth line. Halo CMEs originating from the solar limb can cause geomagnetic storms (*e.g.* Huttunen *et al.*, 2002). According to the statistical study by Gopalswamy *et al.* (2008), about 9 % of large geomagnetic storms are caused by limb halos. Cid *et al.* (2012) also showed that in particular CMEs originating from the western solar limb can be geoeffective because of longitudinal deflection. Lugaz *et al.* (2012) demonstrated that a collision with another CME can cause longitudinal deflection. The authors used white-light and *in-situ* observations to make an estimate of longitudinal deflection of the order of $8^\circ - 10^\circ$. Another example of collision of two CMEs was studied by Shen *et al.* (2012). According to them, the analyzed event resembles the properties of a super-elastic collision, which caused CMEs' deflection and affected their propagation velocities. Rodriguez *et al.* (2011) linked coronagraph observations of a CME and *in-situ* measurements of the associated magnetic cloud for a number of selected events, and they concluded that, in general, predictions of the flux-rope detections near 1 AU based on the coronagraphic data match the actual *in-situ* observations well.

However, in some cases CMEs seemed to have experienced a strong longitudinal deflection in the inner heliosphere.

It is well-established that many CMEs, in particular near solar minimum, tend to deflect towards the solar Equator (Plunkett *et al.*, 2001; Cremades, Bothmer, and Tripathi, 2006; Wang *et al.*, 2011). Shen *et al.* (2011) explained the latitudinal deflection of slow CMEs in the lower corona by interaction with the background magnetic field perturbed by the CME itself. The magnetic-field lines, which go around the CME, become significantly compressed and the free energy from the compression provides a restoring force that acts on the CME, so that the CME tends to deflect into the region with lower magnetic-energy density. However, the density of the heliospheric magnetic field decreases with increasing heliocentric distance, which means that the restoring force is significant only close to the Sun.

Yurchyshyn, Abramenko, and Tripathi (2009) showed in a statistical study of 100 CMEs in the lower corona that there is a slight preference in CME rotation toward the solar equatorial plane and heliospheric current sheet (HCS), and they suggested that the rotation of CMEs is due to the presence of a heliospheric magnetic field. The flux-rope tilt was estimated in that work by fitting an ellipse to halo-CME coronagraph images. Lynch *et al.* (2009) showed in MHD simulations that flux ropes created by flare reconnection undergo significant rotation during their propagation through approximately two R_{\odot} . They also suggested that the rotation effects in the lower corona might be completely washed out or dominated by the larger-scale streamer-belt orientation or coronal-hole structure when the CME evolves to heliospheric sizes. There are numerous proofs of the latter; *e.g.* Vourlidas *et al.* (2011) showed an example of a CME which kept rotating in the inner heliosphere, possibly due to interaction with a fast stream. Yurchyshyn *et al.* (2007), in a study of 25 CME-interplanetary CME pairs, concluded that about one-third of halo CMEs experience rotation of more than 45° during their propagation through interplanetary media from the Sun to the Earth.

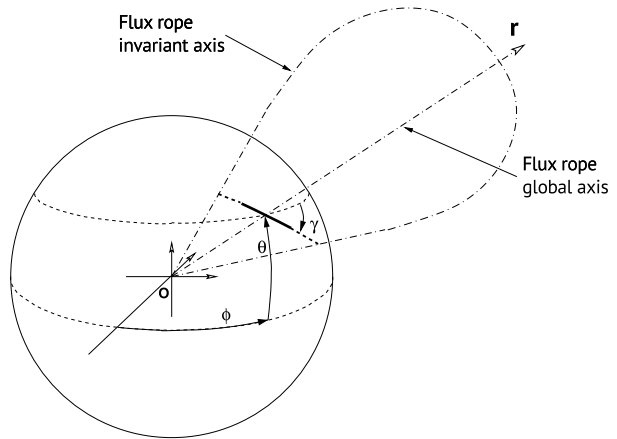
Most of the studies described above analyzed CME evolution by tracing some geometrical parameters without consistency of treating it as a 3D object in 3D space. A detailed analysis of the evolution of a CME as a 3D structure was presented by Isavnin, Vourlidas, and Kilpua (2013) (hereafter referred to as Article I). The authors studied the deflections and rotations of 15 slow CMEs observed during the decay of Solar Cycle 23 and rise of Solar Cycle 24. The analysis verified that the flux ropes tend to deflect toward the solar equatorial plane but they also experience rotation on their way to 1 AU. In the current article (Article II) we extend the technique towards a more precise determination of geometrical parameters of the studied CMEs. We make use of observations of solar sources of CMEs, white-light observations and *in-situ* measurements. In this study we estimate the geometrical evolution of CMEs between $\approx 30 R_{\odot}$ and 1 AU by propagating them as 3D structures through MHD simulated background solar wind. In Article I we used only the average values of solar-wind velocity and CME propagation speed at 1 AU. In this article we mostly focus on CME rotations without neglecting latitudinal and longitudinal deflections. Our technique allows us to study CME evolution in relation to the HCS. We seek answers to the following questions:

- At what heliocentric distances do most of the rotation and deflection of flux ropes occur?
- Why and how do the flux ropes tend to align with the HCS?

2. Methodology

In this section we describe different observational and analytical techniques to trace the flux rope as a 3D structure from its ejection on the Sun to its arrival at 1 AU. The 3D orientation

Figure 1 Scheme of a flux rope ejected from the Sun. The vector \mathbf{r} represents the global axis of the flux rope originating in the Sun and going through the apex of the flux rope. It defines the latitude $[\theta]$ and longitude $[\phi]$ of the flux rope in Stonyhurst coordinates. The rotation of the flux rope around vector \mathbf{r} (a vector from the Sun to the apex of the flux rope) defines the tilt angle $[\gamma]$ of the flux rope. The set of angles $[\theta, \phi, \gamma]$ represents the 3D orientation of the flux rope. (Adapted from Thernisien, Vourlidas, and Howard, 2009.)



of a flux rope is defined by the latitude $[\theta]$ and longitude $[\phi]$ of its global axis and the tilt angle $[\gamma]$ as shown in Figure 1. We use Stonyhurst coordinates.

We estimate the 3D orientation of a flux rope close to the Sun shortly after the moment that it was ejected by determining the tilt of the associated post-eruption arcades or eruptive prominences (Yurchyshyn and Tripathi, 2010 and references therein). The flare model suggested by Forbes (2000) predicts the formation of flare ribbons underneath and parallel to the axis of the erupting flux rope which could be used as proxies of the orientation of the erupted flux rope. Prominence eruptions on the other hand are related to CMEs in a way that part of an erupting filament becomes the bright core of the CME (Gopalswamy *et al.*, 2003). We measure the geometrical orientations of these features using extreme-ultraviolet (EUV) observations provided by *EUV Imaging Telescope* (EIT: Delaboudinière *et al.*, 1995) and *Extreme UltraViolet Imager* (EUVI: Wülser *et al.*, 2004) instruments onboard the *Solar and Heliospheric Observatory* (SOHO: Domingo, Fleck, and Poland, 1995) and *Solar Terrestrial Relations Observatory* (STEREO: Kaiser *et al.*, 2008) spacecraft, respectively.

Next, we use coronagraph observations to trace the flux rope from $\approx 2 R_{\odot}$ to $\approx 30 R_{\odot}$. We use COR1 ($1.5 - 4 R_{\odot}$) and COR2 ($2.5 - 15 R_{\odot}$) coronagraphs of the *Sun Earth Connection Coronal and Heliospheric Investigation* (SECCHI) mission onboard STEREO (Howard *et al.*, 2008) and C2 ($2.2 - 6 R_{\odot}$) and C3 ($3.5 - 30 R_{\odot}$) LASCO coronagraphs onboard SOHO (Brueckner *et al.*, 1995). By combining white-light observations of the same flux rope from different view angles, we take advantage of 3D forward modeling (FM: Thernisien, Vourlidas, and Howard, 2009) to obtain its geometrical parameters.

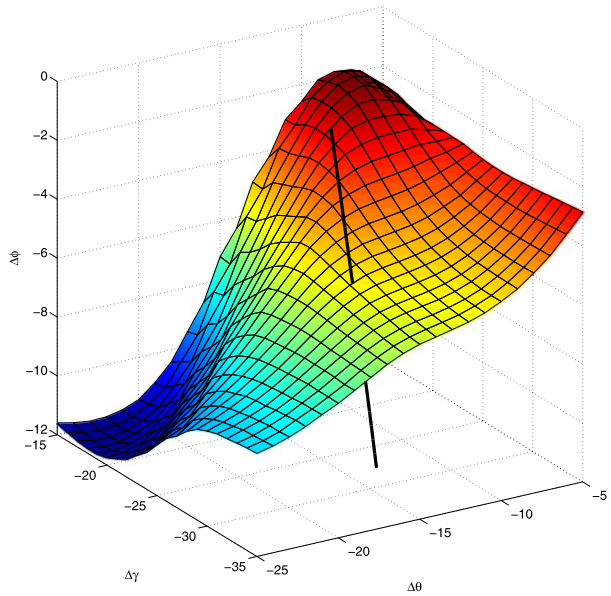
After $\approx 30 R_{\odot}$ we face a problem. Although white-light observations from heliospheric imagers HI-1 and HI-2 are available, a flux rope is not always sufficiently clear to obtain a reliable FM fit.

A method for estimating the amount of deflection and rotation that the flux ropes experience between $\approx 30 R_{\odot}$ to 1 AU was described in Article I. The method used white-light coronagraph observations, *in-situ* measurements of the associated magnetic cloud at 1 AU, and an estimation of the longitudinal deflection as an input. The longitudinal deflection is calculated using the following equation:

$$\Delta\phi = \Omega \left(\frac{1}{V_{FR}} - \frac{1}{V_{SW}} \right) 1 \text{ AU}, \tag{1}$$

which describes the kinetics of the interaction of a flux rope with Parker-spiral-structured solar wind (Wang *et al.*, 2004), where $\Delta\phi$ is longitudinal deflection, Ω is the angular speed

Figure 2 The ensembles of possible solutions for latitudinal and longitudinal deflections and rotation experienced by a flux rope during its travel from $\approx 30 R_{\odot}$ to 1 AU depicted in 3D space $[\Delta\theta, \Delta\phi, \Delta\gamma]$. The black curve represents the solutions for the technique presented in Article I, the surface represents the solutions for the technique presented in Article II (current article). The intersection of the curve and the surface gives the unique set of deflections and rotation $[\Delta\theta, \Delta\phi, \Delta\gamma]$ for the studied event. The color scale is used here to improve visual perception of the plot and corresponds to $\Delta\phi$. The presented plot shows the solutions for event #5 (27 December 2008) in Table 1.



of rotation of the Sun, V_{FR} is the radial velocity of the flux-rope leading edge, and V_{SW} is the solar-wind radial velocity. The underlying assumption is that the magnetic-field strength of the FR-CMEs is weak and comparable to the background magnetic field. This seems an appropriate assumption for our events occurring during an unusually weak solar minimum. For the applicability of the technique, it is necessary that the magnetic cloud associated with the flux rope is measured by one of the STEREO spacecraft or *Wind* spacecraft at 1 AU. Grad–Shafranov reconstruction (GSR: Hu and Sonnerup, 2002; Möstl *et al.*, 2009; Isavnin, Kilpua, and Koskinen, 2011) was used to estimate the flux-rope cross-section at 1 AU. The most important output of GSR in this case is the local orientation of the invariant axis of the flux rope, which acts as a constraint for the global orientation of the flux rope at 1 AU. Assuming that the flux rope expands self-similarly while preserving the hollow-croissant shape described by FM it is possible to establish a unique trigonometrical relation between the longitudinal deflection and a pair of latitudinal deflection and rotation that the structure experiences on its way from $\approx 30 R_{\odot}$ to 1 AU:

$$(\Delta\theta, \Delta\gamma) = f(\Delta\phi), \tag{2}$$

where $\Delta\theta$, $\Delta\phi$, and $\Delta\gamma$ are latitudinal deflection, longitudinal deflection and rotation experienced by a flux rope on the way from $\approx 30 R_{\odot}$ to 1 AU, respectively. The details of the trigonometrical relation (2) are described in Article I. One can think of Equation (2) as a curve in 3D space $[\Delta\theta, \Delta\phi, \Delta\gamma]$ (see Figure 2).

A serious limitation of the technique as presented in Article I is the assumption that the flux-rope leading-edge speed [V_{FR}] and solar-wind radial velocity [V_{SW}] are constant between $\approx 30 R_{\odot}$ and 1 AU. Obviously, the speed of the leading edge and the solar-wind speed can change during propagation. This problem can be solved by converting Equation (1) into integral form:

$$\Delta\phi = \Omega \int_{r_0}^{1AU} \left(\frac{1}{V_{FR}(r)} - \frac{1}{V_{SW}(r)} \right) dr, \tag{3}$$

Table 1 Analysis of the evolution of ejected flux ropes for 14 events. Latitude [θ], longitude [ϕ], and tilt [γ] represent the geometrical orientation of the flux rope at different stages of its evolution. h_{LE} is the height of the leading edge of the flux ropes above the Sun measured in R_{\odot} . V_{FR} is the flux-rope leading-edge speed measured *in-situ* at 1 AU.

#	CME Date	0–2 R_{\odot} (EUVE/IT)			2–8 R_{\odot} (COR1/C2)			8–30 R_{\odot} (COR2/C3)			1 AU				
		θ	γ	h_{LE}	θ	ϕ	γ	θ	ϕ	γ	θ	ϕ	γ	V_{FR}	
1	02 June 2008	-27	5	3.9	-3	-35	-20	-2	-32	-49	17.0	4	-28	-63	397
2	07 July 2008	-42	12	4.2	-20	-16	-6	-19	-22	-2	18.5	-10	-13	-30	561
3	30 August 2008	-37	38	5.1	-12	-2	-4	-10	3	-2	16.9	8	-4	-15	466
4	12 December 2008	41	141	4.6	15	10	76	7	8	63	20.6	-2	8	-17	355
5	27 December 2008	40	5	3.6	20	-23	7	16	-38	14	14.0	3	-50	-14	425
6	27 September 2009	50	-35	3.5	15	-67	7	6	-58	4	10.8	2	-54	-49	362
7	15 January 2010	-42	12	3.9	-3	-82	2	2	-91	7	13.1	-5	-87	26	330
8	01 February 2010	-32	-7	5.6	-21	70	22	-18	65	25	15.6	-5	61	35	402
9	03 April 2010	-25	-10	3.2	-25	7	15	-23	5	9	20.9	-5	-9	-14	750
10	27 May 2010	-43	51	5.8	-10	89	40	-12	73	62	16.4	6	72	-3	408
11	13 June 2010	37	-37	4.1	33	105	-24	20	97	-17	21.6	2	95	-16	500
12	03 November 2010	-22	31	7.9	1	-84	18	-7	-76	11	19.5	5	-81	42	399
13	12 December 2010	-22	28	4.4	-16	60	9	-17	48	6	13.9	6	31	-14	482
14	12 December 2010	-42	50	4.7	-14	-95	-9	-11	-88	-11	20.5	6	-94	2	350

where r_0 is the height at which we start to trace the flux rope; in fact r_0 is the last height where clear white-light observations of the structure from both STEREO spacecraft and SOHO are available. $V_{\text{FR}}(r)$ and $V_{\text{SW}}(r)$ are radial-velocity profiles of the flux-rope leading edge and solar wind along the trajectory of the flux rope, respectively. Equation (3) can be solved numerically if the velocity profiles are known.

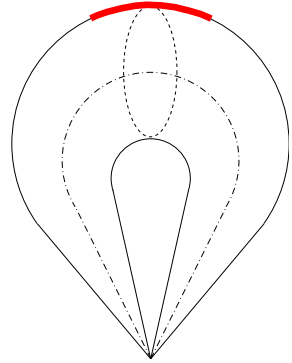
Poomvises, Zhang, and Olmedo (2010) showed that the velocity of the flux-rope leading edge converges quickly in interplanetary space to match the speed of the surrounding solar wind, so that it becomes nearly constant after $50 R_{\odot}$. This result means that CME drag happens during an early stage of CME evolution and implies that the constant speed of the flux-rope leading edge after $50 R_{\odot}$ is a reasonable assumption (Colaninno, Vourlidas, and Wu, 2013). In addition, Kilpua *et al.* (2012) studied Sun-to-Earth travel times of CMEs during the Solar Cycle 23/24 minimum and found that the ICME leading-edge speed measured at 1 AU yielded the best correlation between the predicted and observed travel times. These results justify the usage of the plasma bulk velocity [V_{FR}] measured *in situ* for the associated magnetic cloud at 1 AU as an estimate for the leading-edge speed. Although HI observations are usually too faint for applying FM, the flux-rope leading edge can be observed quite clearly in them using time-elongation maps (J-maps). Using the harmonic-mean approach (HM: Lugaz, Vourlidas, and Roussev, 2009) it is possible to estimate the average speed of the leading edge of the flux rope and its propagation direction by assuming that the leading edge of the flux rope is spherical. Whenever the geometrical configuration of spacecraft makes it possible, we apply the HM approach with fixed propagation direction obtained with FM at $\approx 30 R_{\odot}$ and compare the estimated leading edge speed with the *in-situ* speed at 1 AU. Thus we ensure that the use of the leading-edge speed measured *in situ* at 1 AU as an estimate for the speed of its propagation from $\approx 30 R_{\odot}$ to 1 AU is a reasonable assumption.

We use the results of global 3D MHD simulations carried out with the MAS (Magnetohydrodynamics Around a Sphere) model (Mikić *et al.*, 1999; Linker *et al.*, 1999; Riley, 2007; Riley *et al.*, 2011) and provided by the Predictive Science STEREO modeling support project (imhd.net/STEREO) as an estimation for the radial velocity of the solar wind [$V_{\text{SW}}(r)$]. The MAS model uses a photospheric magnetic-field map built up from a sequence of observations centered at central meridian over a 27-day period as an input. The resulting global simulation does not include the expanding flux rope and thus the resulting solar wind is not yet perturbed and can be considered as background solar wind. The model is calculated once per Carrington rotation. Thus, it does not take into account solar-wind streams' evolution during one Carrington rotation. This is not so crucial during the solar-minimum period covered by our observations. The use of outdated photospheric magnetic-field information would make the results of MHD simulations less reliable during solar maximum when the configuration of magnetic field is subject to frequent and rapid changes. The photospheric magnetic-field map measured during one full Carrington rotation uses the newest data for the western heliosphere and the oldest for the eastern heliosphere which makes the MHD-simulated background solar wind less reliable for the eastern heliosphere and introduces uncertainties in the analysis.

Now that the flux-rope expansion velocity and background solar-wind velocity are estimated, we can solve Equation (3) numerically. Equation (3) describes only longitudinal deflection of the flux rope. We solve it for the range of possible latitudinal deflection and rotation angles [$\Delta\theta$ and $\Delta\gamma$], respectively. For simplicity we assume that θ and γ change linearly from r_0 to 1 AU:

$$\theta(r) = \theta(r_0) + \Delta\theta \frac{r - r_0}{1 \text{ AU} - r_0}, \quad (4)$$

Figure 3 The scheme of the flux rope. The thick red curve shows the part of the leading edge that we are tracing through the background solar wind. The radial velocity of the background solar wind is averaged along the leading edge of the flux rope.



$$\gamma(r) = \gamma(r_0) + \Delta\gamma \frac{r - r_0}{1 \text{ AU} - r_0}. \quad (5)$$

We do not assume a point object for the FR tracing. Instead we trace the front part of its leading edge as shown in Figure 3. In each integration step $[n]$ we calculate the longitude $[\phi_n]$ of the flux rope with the following equation:

$$\phi_n = \phi_{n-1} + \Omega \left(\frac{1}{V_{\text{FR}}(r_n)} - \frac{1}{\tilde{V}_{\text{SW}}(r_n)} \right) (r_n - r_{n-1}), \quad (6)$$

where $\tilde{V}_{\text{SW}}(r_n)$ is the background solar-wind radial velocity averaged along the part of the leading edge of the flux rope as depicted in Figure 3. The background solar wind simulated with the MAS model for one Carrington rotation is static, *i.e.* no dynamic outflow is simulated. If we assume that the photospheric magnetic field has a stationary configuration then the steady outflow of the solar wind can be modeled by rotating the MHD-simulated solar wind as a 3D object with the solar angular-rotation speed $[\Omega]$. The rotation is taken into account in each integration step.

The described technique can be represented with the following equation:

$$\Delta\phi = g(\Delta\theta, \Delta\gamma). \quad (7)$$

Equation (7) describes also a surface in 3D space $[\Delta\theta, \Delta\phi, \Delta\gamma]$ (see Figure 2).

Finally, we combine the two techniques. The intersection of the curve described by Equation (2) and the surface described by Equation (7) define the unique set of longitudinal and latitudinal deflections and rotation of the flux rope that is the solution for both methods simultaneously as shown in Figure 2.

To recap, we use the following methodology to trace ejected flux ropes from the Sun to 1 AU. First, we use extreme-ultraviolet observations of flux-rope signatures close to the solar surface to estimate the initial orientation of the FR. Then, we use multipoint white-light observations to model the flux rope with FM from $\approx 2 R_{\odot}$ to $\approx 30 R_{\odot}$. Finally, we trace the flux rope through the MHD-simulated solar wind from $\approx 30 R_{\odot}$ to 1 AU using *in-situ* measurements of the associated magnetic cloud as a local constraint for the global orientation of the flux rope.

3. Results

We examine the 14 events during the decay of Solar Cycle 23 and rise of Solar Cycle 24 presented in Article I with this technique. We deduce 3D orientation of flux ropes in several

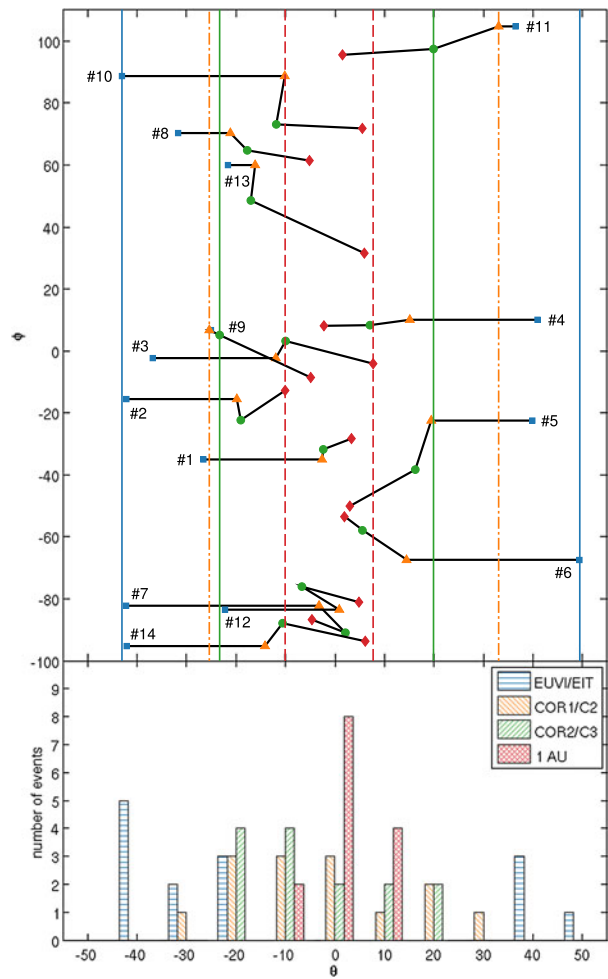
points during their propagation. Therefore, unlike Article I, we always have an estimate of the direction of rotation of flux ropes. The results are presented in Table 1. The orientation (latitude and longitude) is given in Stonyhurst coordinates (see Figure 1). The EUVI/EIT part of Table 1 represents the EUV observations on the solar disk and estimations of the flux-rope orientation using post-eruption arcades or eruptive prominences. The longitudinal expansion of these structures is often unclear, so we estimate only longitude and tilt angle from those observations. The COR1/C2 part of Table 1 corresponds to the FM results of white-light images of flux ropes in the field of view of COR1 and C2 coronagraphs. The values of latitude, longitude, and tilt angle are averages of the FM parameters. The average height of the center of the leading edge of the flux rope was in the range of 3 to 8 R_{\odot} for those observations. Similarly, the COR2/C3 part of the Table 1 corresponds to the average 3D orientation of flux ropes in the field of view of COR2 and C3 coronagraphs with average height of the center of the leading edge of 10 to 22 R_{\odot} . The 1 AU part of Table 1 corresponds to the results of the flux-rope propagation technique that was described in Section 2. The total latitudinal deflections experienced by flux ropes from the Sun to 1 AU ranged from 20° to 49°, the total longitudinal deflections ranged from -28° to 14°, and the total rotations ranged from 4° to 164°.

Figures 4 and 5 display the results given in Table 1. Figure 4 shows the longitudinal and latitudinal deflections of the 14 flux ropes. The markers on the plot correspond to the orientation of the vector from the Sun to the apex of the flux rope. Figure 4 confirms that the flux ropes tend to deflect towards the solar equatorial plane. Close to the Sun, the flux ropes fall within the range of latitudes $[-42^{\circ}; 50^{\circ}]$, at $\approx 5 R_{\odot}$ the range shrinks to $[-25^{\circ}; 33^{\circ}]$, at $\approx 18 R_{\odot}$ it shrinks further to $[-22^{\circ}; 20^{\circ}]$, and finally at 1 AU the flux ropes fall within the range of latitudes of $[-10^{\circ}; 8^{\circ}]$. The longitudinal deflections between $\approx 5 R_{\odot}$ and 1 AU ranged from -29° to 14° . For some of the events the direction of longitudinal deflection changed on the way to 1 AU (e.g. #2, #3, #7). Such behavior can be caused by structural variability of the solar wind, e.g. a flux rope moved in the fast solar wind and then entered an area with slower solar wind. These deviations could be also due to misidentification of source regions, erroneous FM fits, and uncertainties of GSR.

To investigate the amount of rotation and deflection at different heliospheric distances we divide the Sun–Earth distance into three segments. The segments chosen are the following: 1–5 R_{\odot} (from EUVI/EIT to COR1/C2 observations), 5–30 R_{\odot} (from COR1/C2 to COR2/C3 observations), and 30–215 R_{\odot} (from COR2/C3 to *in-situ* observations). Figure 5 shows that flux-rope geometrical evolution happens fast in the lower corona, i.e. $\approx 41\%$ of estimated flux-rope rotation and $\approx 48\%$ of latitudinal deflection happens during the first 3% ($\approx 5 R_{\odot}$) of the path from the Sun to 1 AU. During the first $\approx 30 R_{\odot}$ of the travel, the flux ropes experience, on average, $\approx 57\%$ of total rotation, $\approx 62\%$ of total latitudinal deflection, and $\approx 58\%$ of total longitudinal deflection. However, it is important to note that a significant amount of deflection and rotation happens in the inner heliosphere from 30 R_{\odot} to 1 AU. The flux-rope evolution after $\approx 30 R_{\odot}$ could be caused by several effects: the flux ropes may change their orientation because the initial momentum gained due to magnetic interactions in the lower corona is sufficient to influence the flux-rope evolution in the inner heliosphere; the decreasing magnetic interaction with the solar magnetic field could become dominated by the kinematic interaction with solar streams in the inner heliosphere; the MHD models may not be sufficiently accurate.

We use constant heliocentric distance slices of the 3D MAS MHD model to study the rotation of flux ropes relative to the local orientation of HCS. Figures 6 and 7 show six events from our study. Each example is presented with three panels corresponding to the heights of the flux-rope leading edge at 2–8 R_{\odot} , 8–30 R_{\odot} , and 1 AU, respectively. The radial

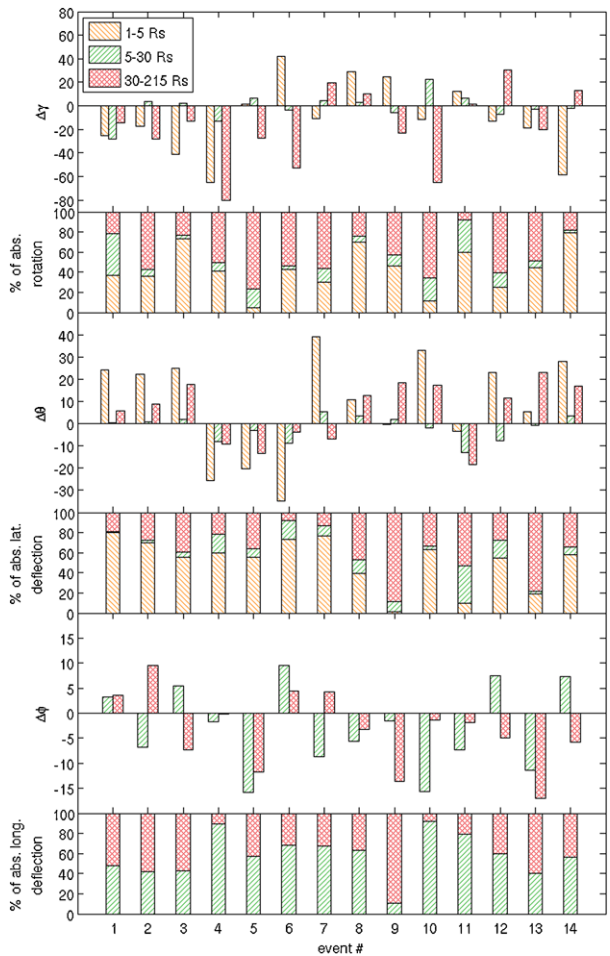
Figure 4 Latitudinal and longitudinal deflections of 14 analyzed flux ropes (top) and distributions of latitudinal deflections for different heights (bottom). The markers represent the direction of the vector from the Sun to the apex of the flux rope in Stonyhurst coordinates. Blue squares correspond to $1-2 R_{\odot}$, orange triangles correspond to $2-8 R_{\odot}$, green circles correspond to $8-30 R_{\odot}$, red diamonds correspond to 1 AU. Blue, orange, red, and green lines show latitudinal ranges for flux-rope orientation at respective heliocentric heights. Note that even though a substantial part of flux-rope deflection happens in the lower corona, the flux ropes' orientation continues to evolve in the inner heliosphere.



component of the background solar-wind velocity is color-coded. The local HCS orientation is depicted with the white dashed curve, which is estimated as the boundary of the area where the radial component of the background magnetic field is zero. The orientations of flux ropes are shown with white ellipses. The position and tilt of each ellipse depict the geometrical orientation of a flux rope. The size of an ellipse gives an idea about the angular width of a flux rope. It can be seen that the local shape of the HCS is too complex to allow an estimate of the flux-rope tilt relative to the HCS with a single value. So we analyze each event by assessing individually images similar to Figures 6 and 7.

What can be noticed from Figures 6 and 7 is that the flux ropes tend to stay close to the HCS until 1 AU although they are not usually strictly aligned with the local HCS. The radial velocity of the background solar wind becomes more structured with increasing heliocentric distance thus creating well-defined slow and fast solar-wind channels. A wide channel of slow wind is typically formed in the vicinity of the HCS, and our flux ropes (which are relatively slow) expand inside this channel. The orientation of flux ropes inside the slow solar-wind channels seems to be defined by the combination of the channel boundaries itself and those of faster streams inside the channel. Depending on the geometry of the slow

Figure 5 The evolution of orientations of the 14 studied flux ropes during the following segments of their travel from the Sun to 1 AU: 1–5 R_{\odot} , 5–30 R_{\odot} , 30 R_{\odot} –1 AU. Panels 1, 3, and 5 show the change of tilt angle, latitude, and longitude, respectively. Panels 2, 4, and 6 show what part of the overall evolution a flux rope experienced during each segment.



solar-wind channel and faster streams inside it the resulting flux-rope configurations can be classified into three groups: flux ropes that are strongly affected by faster streams, and thus not aligned with the HCS (Figure 6, left); flux ropes that are influenced by faster streams but stay close to the HCS (Figure 7, right); flux ropes that stay aligned with the HCS and are not affected strongly enough by faster streams to change their orientation (Figure 6, right; Figure 7, left).

Event #3 (Figure 6, left) belongs to the first group of events in our classification. It seems that the fast solar-wind stream isolates or compresses a part of the slow solar-wind channel with the flux trapped in it. The magnetic-energy density map (Figure 6, left, bottom panel) shows magnetic compression in the region between the fast stream and the flux rope, which could be a signature of their interaction. Note also that the flux rope appears to have crossed over the HCS at 1 AU, which implies that magnetic interactions with the HCS are weak far from the Sun.

Event #12 (Figure 6, right) demonstrate the flux rope with orientation at 1 AU influenced by the structured background solar wind. A fast solar-wind stream could be a possible reason for the origin of compression region between the stream and the flux rope (Figure 6, right,

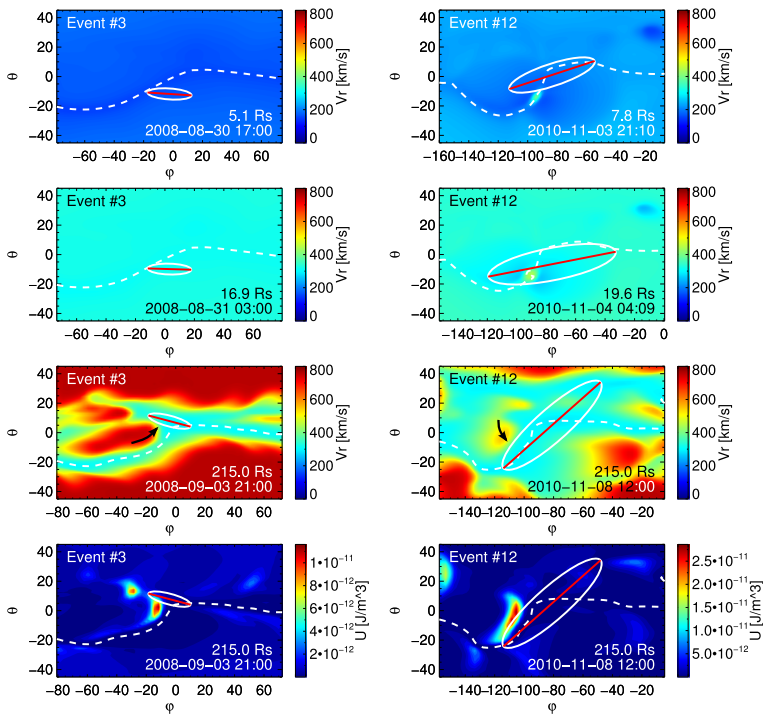


Figure 6 Maps of the radial component of the background solar wind (top three panels, color-coded), magnetic-energy density (bottom panel, color-coded), and HCS (white dashed curve). The orientation of a flux rope is represented by an ellipse. The size of an ellipse corresponds to the angular size of a flux rope. The black arrows show the approximate direction of momentum acting on flux ropes due to magnetic-energy density gradient. Upper three panels correspond to the heights of $2\text{--}8 R_{\odot}$, $8\text{--}30 R_{\odot}$, and 1 AU , respectively. Bottom panels show the magnetic-energy density at 1 AU . Events #3 (left) and #7 (right) are presented.

bottom panel). The flux rope stays close to the HCS but it is not completely aligned with it due to interaction with the faster stream.

The flux ropes that correspond to Event #7 (Figure 7, left) and Event #11 (Figure 7, right) seem to align well with the HCS at 1 AU . This can lead to an assumption that these flux ropes were attracted to the HCS due to magnetic interaction. However, the hypothesis of the interaction with the background magnetic field explains the positioning of these flux ropes as well, *i.e.* the flux ropes were pushed into the zone of lower magnetic-energy density.

Closer to the Sun ($\leq 30 R_{\odot}$) the radial velocity of background solar wind is more uniform, and we do not see any obvious interactions with background solar wind in the first two panels of Figures 6 and 7. However, flux ropes tend to stay close to the HCS. This behavior supports the suggestion that close to the Sun the magnetic interactions influence the orientation a flux rope. However, as the flux rope propagates further from the Sun the disturbance of the surrounding magnetic field created by it gets weaker and eventually the interactions with solar-wind streams become the dominant factor influencing the orientation and evolution of the flux rope. The fact that our flux ropes were located close to the HCS in the first place points to either an origin close to the HCS or to strong deflection towards the HCS in the low corona.

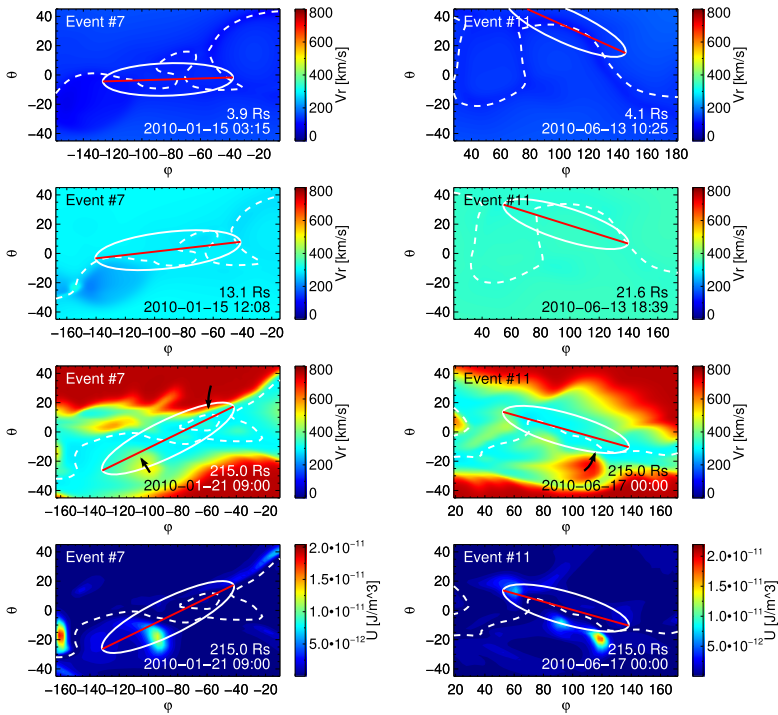


Figure 7 Maps of the radial component of the background solar wind (top three panels, color-coded), magnetic-energy density (bottom panel, color-coded), and HCS (white dashed curve). The orientation of a flux rope is represented by an ellipse. The size of an ellipse corresponds to the angular size of a flux rope. The black arrows show the approximate direction of momentum acting on flux ropes due to magnetic-energy density gradient. Upper three panels correspond to the heights of 2–8 R_{\odot} , 8–30 R_{\odot} , and 1 AU, respectively. Bottom panels show the magnetic-energy density at 1 AU. Events #11 (left) and #12 (right) are presented.

4. Discussion

In this article we describe a technique for studying the 3D evolution of ejected flux ropes from the Sun to 1 AU. The method uses EUV and white-light observations from SOHO and STEREO and *in-situ* measurements at 1 AU from *Wind* and STEREO. The results of MHD simulations made with the MAS model provided an estimate of the background solar wind when tracing flux ropes from $\approx 30 R_{\odot}$ to 1 AU. GSR is used to estimate the local orientations of flux ropes at 1 AU which in turn is used as a constraint for their global orientations. An example of FM analysis of white-light observations and GSR analysis of *in-situ* measurements for the Event #12 was presented in Article I (Figures 3 and 4).

Using this method we studied 14 ejected flux ropes observed during the decay of Solar Cycle 23 and early rise of Solar Cycle 24. Our analysis confirmed that flux ropes tend to deflect towards the solar equatorial plane, and we quantified the amount of deflection at different heliocentric distances. We find that a large part of the latitudinal deflection occurs within a few R_{\odot} . Thus, magnetic interactions with nearby coronal holes may be the main cause of latitudinal deflection (Shen *et al.*, 2011). Our results show that about 60 % of the geometrical evolution of flux ropes happens within the first 30 R_{\odot} . Nevertheless, a significant part of the deflection and rotation occurs between 30 R_{\odot} and 1 AU, *i.e.* outside the current coronagraphs' fields of view.

We also study the rotation of the flux ropes relative to the HCS. As expected, we find that the flux ropes stay close the HCS but they are not necessarily aligned with it. Some non-alignments seem to be influenced by the relative location of fast- and slow-wind streams (e.g. Figure 6 (right)) while others may be due to modeling errors. However, the latter should be minimal as our analysis extends over one of the deepest solar minima on record.

We studied the evolution of slow solar flux ropes during the low solar-activity phase in Article I and here to develop a technique for tracing flux ropes from the Sun to 1 AU. We expect that faster flux ropes, observed more frequently during solar-maximum conditions, should experience higher degrees of distortion and longitudinal eastward deflection when propagating through slower background solar wind. The differential background solar wind can also be responsible for distortion of flux ropes. Savani *et al.* (2010) studied a CME that was distorted into a concave structure apparently due to kinematic interaction with slow solar wind. Such distortion should be more pronounced for fast CMEs since the drag on the CME is stronger. If the background solar wind is highly structured the drag force will be different for different parts of the flux ropes, causing distortion.

Acknowledgements The work of AI and EK was supported by the Academy of Finland. The work of AV is supported by NASA contract S-136361-Y to the Naval Research Laboratory. LASCO was constructed by a consortium of institutions: NRL (USA), MPI für Aeronomie (Germany), LAS (France), and University of Birmingham (UK). The SECCHI data are produced by an international consortium of the NRL, LMSAL, and NASA GSFC (USA), RAL and University of Birmingham (UK), MPS (Germany), CSL (Belgium), IOTA, and IAS (France).

References

- Brueckner, G.E., Howard, R.A., Koomen, M.J., Korendyke, C.M., Michels, D.J., Moses, J.D., Socker, D.G., Dere, K.P., Lamy, P.L., Llebaria, A., Bout, M.V., Schwenn, R., Simnett, G.M., Bedford, D.K., Eyles, C.J.: 1995, The large angle spectroscopic coronagraph (LASCO). *Solar Phys.* **162**, 357. doi:[10.1007/BF00733434](https://doi.org/10.1007/BF00733434).
- Chen, P.F.: 2011, Coronal mass ejections: Models and their observational basis. *Living Rev. Solar Phys.* **8**(1). doi:[10.12942/lrsp-2011-1](https://doi.org/10.12942/lrsp-2011-1).
- Cid, C., Cremades, H., Aran, A., Mandrini, C., Sanahuja, B., Schmieder, B., Menvielle, M., Rodriguez, L., Saiz, E., Cerrato, Y., Dasso, S., Jacobs, C., Lathuillere, C., Zhukov, A.: 2012, Can a halo CME from the limb be geoeffective? *J. Geophys. Res.* **117**, A11102. doi:[10.1029/2012JA017536](https://doi.org/10.1029/2012JA017536).
- Colaninno, R.C., Vourlidas, A., Wu, C.C.: 2013, Quantitative comparison of methods for predicting the arrival of coronal mass ejections at Earth based on multiview imaging. *J. Geophys. Res.* **118**, 6866. doi:[10.1002/2013JA019205](https://doi.org/10.1002/2013JA019205).
- Cremades, H., Bothmer, V., Tripathi, D.: 2006, Properties of structured coronal mass ejections in solar cycle 23. *Adv. Space Res.* **38**, 461. doi:[10.1016/j.asr.2005.01.095](https://doi.org/10.1016/j.asr.2005.01.095).
- Delaboudinière, J.P., Artzner, G.E., Brunaud, J., Gabriel, A.H., Hochedez, J.F., Millier, F., Song, X.Y., Au, B., Dere, K.P., Howard, R.A., Kreplin, R., Michels, D.J., Moses, J.D., Defise, J.M., Jamar, C., Rochus, P., Chauvineau, J.P., Marioge, J.P., Catura, R.C., Lemen, J.R., Shing, L., Stern, R.A., Gurman, J.B., Neupert, W.M., Maucherat, A., Clette, F., Cugnon, P., Dessel, E.L.: 1995, EIT: extreme-ultraviolet imaging telescope for the SOHO mission. *Solar Phys.* **162**, 291. doi:[10.1007/BF00733432](https://doi.org/10.1007/BF00733432).
- Domingo, V., Fleck, B., Poland, A.I.: 1995, The SOHO mission: An overview. *Solar Phys.* **162**, 1. doi:[10.1007/BF00733425](https://doi.org/10.1007/BF00733425).
- Forbes, T.G.: 2000, A review on the genesis of coronal mass ejections. *J. Geophys. Res.* **105**(A10), 23153. doi:[10.1029/2000JA000005](https://doi.org/10.1029/2000JA000005).
- Gopalswamy, N., Lara, A., Yashiro, S., Nunes, S., Howard, R.A.: 2003, Coronal mass ejection activity during solar cycle 23. In: Wilson, A. (ed.) *Solar Variability as an Input to the Earth's Environment* **SP-535**, 403.
- Gopalswamy, N., Mäkelä, P., Xie, H., Akiyama, S., Yashiro, S.: 2009, CME interactions with coronal holes and their interplanetary consequences. *J. Geophys. Res.* **114**, A00A22. doi:[10.1029/2008JA013686](https://doi.org/10.1029/2008JA013686).
- Gopalswamy, N., Yashiro, S., Xie, H., Akiyama, S., Mäkelä, P.: 2008, Large geomagnetic storms associated with limb halo coronal mass ejections. *Adv. Geosci.* **21**.

- Howard, R.A., Moses, J.D., Vourlidas, A., Newmark, J.S., Socker, D.G., Plunkett, S.P., Korendyke, C.M., Cook, J.W., Hurlley, A., Davila, J.M., Thompson, W.T., St Cyr, O.C., Mentzell, E., Mehalick, K., Lemen, J.R., Wuelser, J.P., Duncan, D.W., Tarbell, T.D., Wolfson, C.J., Moore, A., Harrison, R.A., Waltham, N.R., Lang, J., Davis, C.J., Eyles, C.J., Mapson-Menard, H., Simnett, G.M., Halain, J.P., Defise, J.M., Mazy, E., Rochus, P., Mercier, R., Ravet, M.F., Delmotte, F., Auchere, F., Delaboudinière, J.P., Bothmer, V., Deutsch, W., Wang, D., Rich, N., Cooper, S., Stephens, V., Maahs, G., Baugh, R., McMullin, D., Carter, T.: 2008, Sun Earth connection coronal and heliospheric investigation (SECCHI). *Space Sci. Rev.* **136**, 67. doi:[10.1007/s11214-008-9341-4](https://doi.org/10.1007/s11214-008-9341-4).
- Hu, Q., Sonnerup, B.U.Ö.: 2002, Reconstruction of magnetic clouds in the solar wind: Orientations and configurations. *J. Geophys. Res.* **107**, 1142. doi:[10.1029/2001JA000293](https://doi.org/10.1029/2001JA000293).
- Huttunen, K.E.J., Koskinen, H.E.J., Pulkkinen, T.I., Pulkkinen, A., Palmroth, M., Reeves, E.G.D., Singer, H.J.: 2002, April 2000 magnetic storm: Solar wind driver and magnetospheric response. *J. Geophys. Res.* **107**(A12), 1440. doi:[10.1029/2001JA009154](https://doi.org/10.1029/2001JA009154).
- Isavnin, A., Kilpua, E.K.J., Koskinen, H.E.J.: 2011, Grad-Shafranov reconstruction of magnetic clouds: Overview and improvements. *Solar Phys.* **273**, 205. doi:[10.1007/s11207-011-9845-z](https://doi.org/10.1007/s11207-011-9845-z).
- Isavnin, A., Vourlidas, A., Kilpua, E.K.J.: 2013, Three-dimensional evolution of ejected flux ropes from the Sun (2–20 R_⊙) to 1 AU. *Solar Phys.* **284**, 203. doi:[10.1007/s11207-012-0214-3](https://doi.org/10.1007/s11207-012-0214-3).
- Kaiser, M.L., Kucera, T.A., Davila, J.M., Cyr, O.C.S., Guhathakurta, M., Christian, E.: 2008, The STEREO mission: An introduction. *Space Sci. Rev.* **136**, 5. doi:[10.1007/s11214-007-9277-0](https://doi.org/10.1007/s11214-007-9277-0).
- Kilpua, E.K.J., Mierla, M., Rodriguez, L., Zhukov, A.N., Srivastava, N., West, M.J.: 2012, Estimating travel times of coronal mass ejections to 1 AU using multi-spacecraft coronagraph data. *Solar Phys.* **279**, 477. doi:[10.1007/s11207-012-0005-x](https://doi.org/10.1007/s11207-012-0005-x).
- Linker, J.A., Mikic, Z., Biesecker, D.A., Forsyth, R.J., Gibson, S.E., Lazarus, A.J., Lecinski, A., Riley, P., Szabo, A., Thompson, B.J.: 1999, Magnetohydrodynamic modeling of the solar corona during whole Sun month. *J. Geophys. Res.* **104**(A5), 9809. doi:[10.1029/1998JA900159](https://doi.org/10.1029/1998JA900159).
- Lugaz, N., Vourlidas, A., Roussev, I.I.: 2009, Deriving the radial distances of wide coronal mass ejections from elongation measurements in the heliosphere – application to CME-CME interaction. *Ann. Geophys.* **27**, 3479. doi:[10.5194/angeo-27-3479-2009](https://doi.org/10.5194/angeo-27-3479-2009).
- Lugaz, N., Farrugia, C.J., Davies, J.A., Möstl, C., Davis, C.J., Roussev, I.I., Temmer, M.: 2012, The deflection of the two interacting coronal mass ejections of 2010 May 23–24 as revealed by combined *in situ* measurements and heliospheric imaging. *Astrophys. J.* **759**. doi:[10.1088/0004-637X/759/1/68](https://doi.org/10.1088/0004-637X/759/1/68).
- Lynch, B.J., Antiochos, S.K., Li, Y., Luhmann, J.G., DeVore, C.R.: 2009, Rotation of coronal mass ejections during eruption. *Astrophys. J.* **697**, 1918. doi:[10.1088/0004-637X/697/2/1918](https://doi.org/10.1088/0004-637X/697/2/1918).
- Mikić, Z., Linker, J.A., Dalton, S.D., Lionello, R., Tarditi, A.: 1999, Magnetohydrodynamic modeling of the global solar corona. *Phys. Plasmas* **6**, 2217. doi:[10.1063/1.873474](https://doi.org/10.1063/1.873474).
- Möstl, C., Farrugia, C.J., Biernat, H.K., Leitner, M., Kilpua, E.K.J., Galvin, A.B., Luhmann, J.G.: 2009, Optimized Grad-Shafranov reconstruction of a magnetic cloud using STEREO-Wind observations. *Solar Phys.* **256**, 427. doi:[10.1007/s11207-009-9360-7](https://doi.org/10.1007/s11207-009-9360-7).
- Nieves-Chinchilla, T., Colaninno, R., Vourlidas, A., Szabo, A., Lepping, R.P., Boardsen, S.A., Anderson, B.J., Korth, H.: 2012, Remote and *in situ* observations of an unusual Earth-directed coronal mass ejection from multiple viewpoints. *J. Geophys. Res.* **117**, A6. doi:[10.1029/2011JA017243](https://doi.org/10.1029/2011JA017243).
- Plunkett, S.P., Thompson, B.J., St Cyr, O.C., Howard, R.A.: 2001, Solar source regions of coronal mass ejections and their geomagnetic effects. *J. Atmos. Solar-Terr. Phys.* **63**, 389. doi:[10.1016/S1364-6826\(00\)00166-8](https://doi.org/10.1016/S1364-6826(00)00166-8).
- Poomvises, W., Zhang, J., Olmedo, O.: 2010, Coronal mass ejection propagation and expansion in three-dimensional space in the heliosphere based on STEREO/SECCHI observations. *Astrophys. J. Lett.* **717**, L159. doi:[10.1088/2041-8205/717/2/L159](https://doi.org/10.1088/2041-8205/717/2/L159).
- Riley, P.: 2007, Modeling corotating interaction regions: From the Sun to 1 AU. *J. Atmos. Solar-Terr. Phys.* **69**, 32. doi:[10.1016/j.jastp.2006.06.008](https://doi.org/10.1016/j.jastp.2006.06.008).
- Riley, P., Lionello, R., Linker, J.A., Mikic, Z., Luhmann, J., Wijaya, J.: 2011, Global MHD modeling of the solar corona and inner heliosphere for the whole heliospheric interval. *Solar Phys.* **274**, 361. doi:[10.1007/s11207-010-9698-x](https://doi.org/10.1007/s11207-010-9698-x).
- Rodriguez, L., Mierla, M., Zhukov, A.N., West, M., Kilpua, E.: 2011, Linking of remote-sensing and *in situ* observations of CMEs using STEREO. *Solar Phys.* **270**, 561. doi:[10.1007/s11207-011-9784-8](https://doi.org/10.1007/s11207-011-9784-8).
- Savani, N.P., Owens, M.J., Rouillard, A.P., Forsyth, R.J., Davies, J.A.: 2010, Observational evidence of a coronal mass ejection distortion directly attributable to a structured solar wind. *Astrophys. J. Lett.* **714**, L128. doi:[10.1088/2041-8205/714/1/L128](https://doi.org/10.1088/2041-8205/714/1/L128).
- Shen, C., Wang, Y., Gui, B., Ye, P., Wang, S.: 2011, Kinematic evolution of a slow CME in corona viewed by STEREO-B on 8 October 2007. *Solar Phys.* **269**, 389. doi:[10.1007/s11207-011-9715-8](https://doi.org/10.1007/s11207-011-9715-8).
- Shen, C., Wang, Y., Wang, S., Liu, Y., Liu, R., Vourlidas, A., Miao, B., Ye, P., Liu, J., Zhou, Z.: 2012, Super-elastic collision of large-scale magnetized plasmoids in the heliosphere. *Nat. Phys.* **8**, 923. doi:[10.1038/nphys2440](https://doi.org/10.1038/nphys2440).

- Thernisien, A., Vourlidas, A., Howard, R.A.: 2009, Forward modeling of coronal mass ejections using STEREO/SECCHI data. *Solar Phys.* **256**, 111. doi:[10.1007/s11207-009-9346-5](https://doi.org/10.1007/s11207-009-9346-5).
- Tsurutani, B.T., Gonzalez, W.D., Tang, F., Akasofu, S.I., Smith, E.J.: 1988, Origin of interplanetary southward magnetic fields responsible for major magnetic storms near solar maximum (1978–1979). *J. Geophys. Res.* **93**(A8), 8519. doi:[10.1029/JA093iA08p08519](https://doi.org/10.1029/JA093iA08p08519).
- Vourlidas, A., Colaninno, R., Noeves-Chinchilla, T., Stenborg, G.: 2011, The first observation of a rapidly rotating coronal mass ejection in the middle corona. *Astrophys. J. Lett.* **733**, L23. doi:[10.1088/2041-8205/733/2/L23](https://doi.org/10.1088/2041-8205/733/2/L23).
- Vourlidas, A., Lynch, B.J., Howard, R.A., Li, Y.: 2012, How many CMEs have flux ropes? Deciphering the signatures of shocks, flux ropes, and prominences in coronagraph observations of CMEs. *Solar Phys.* **284**, 179. doi:[10.1007/s11207-012-0084-8](https://doi.org/10.1007/s11207-012-0084-8).
- Wang, Y., Shen, C., Wang, S., Ye, P.: 2004, Deflection of coronal mass ejection in the interplanetary medium. *Solar Phys.* **222**, 329. doi:[10.1023/B:SOLA.0000043576.21942.aa](https://doi.org/10.1023/B:SOLA.0000043576.21942.aa).
- Wang, Y., Chen, C., Gui, B., Shen, C., Ye, P., Wang, S.: 2011, Statistical study of coronal mass ejection source locations: Understanding CMEs viewed in coronagraphs. *J. Geophys. Res.* **116**, A04104. doi:[10.1029/2010JA016101](https://doi.org/10.1029/2010JA016101).
- Wülser, J.P., Lemen, J.R., Tarbell, T.D., Wolfson, C.J., Cannon, J.C., Carpenter, B.A., Duncan, D.W., Gradwohl, G.S., Meyer, S.B., Moore, A.S., Navarro, R.L., Pearson, J.D., Rossi, G.R., Springer, L.A., Howard, R.A., Moses, J.D., Newmark, J.S., Delaboudinière, J.P., Artzner, G., Auchère, F., Bougnet, M., Bouyries, P., Bridou, F., Clotaire, J.Y., Colas, G., Delmotte, F., Jerome, A., Lamare, M., Mercier, R., Mullet, M., Ravet, M.F., Song, X., Bothmer, V., Deutsch, W.: 2004, EUVI: The STEREO-SECCHI extreme ultraviolet imager. In: Fineschi, S., Gummin, M.A. (eds.) *Proc. SPIE* **5171**. doi:[10.1117/12.506877](https://doi.org/10.1117/12.506877).
- Yurchyshyn, V., Abramenko, V., Tripathi, D.: 2009, Rotation of white-light coronal mass ejection structures as inferred from LASCO coronagraph. *Astrophys. J.* **705**, 426. doi:[10.1088/0004-637X/705/1/426](https://doi.org/10.1088/0004-637X/705/1/426).
- Yurchyshyn, V., Tripathi, D.: 2010, Relationship between Earth-directed solar eruptions and magnetic clouds at 1 AU: A brief review. *Adv. Geosci.* **21**, 51.
- Yurchyshyn, V., Hu, Q., Lepping, R.P., Lynch, D.J., Krall, J.: 2007, Orientations of LASCO halo CMEs and their connection to the flux rope structure of interplanetary CMEs. *Adv. Space Res.* **40**, 1821. doi:[10.1016/j.asr.2007.01.059](https://doi.org/10.1016/j.asr.2007.01.059).
- Zhang, J., Richardson, I.G., Webb, D.F., Gopalswamy, N., Huttunen, E., Kasper, J.C., Nitta, N.V., Poomvises, W., Thompson, B.J., Wu, C.C., Yashiro, S., Zhukov, A.N.: 2007, Solar and interplanetary sources of major geomagnetic storms ($Dst \leq -100$ nT) during 1996–2005. *J. Geophys. Res.* **112**, A10102. doi:[10.1029/2007JA012321](https://doi.org/10.1029/2007JA012321).